JGR Solid Earth

RESEARCH ARTICLE
10.1029/2018JB016553

# Linking Structural and Transport Properties in Three-Dimensional Fracture Networks

**J. D. Hyman[1], M. Dentz[2], A. Hagberg[3], and P. K. Kang[4]**

[1]Computational Earth Science (EES-16), Earth and Environmental Sciences Division, Los Alamos National Laboratory, Los Alamos, NM, USA, [2]Spanish National Research Council (IDAEA-CSIC), Barcelona, Spain, [3]Computer, Computational, and Statistical Sciences Division, Los Alamos National Laboratory, Los Alamos, NM, USA, [4]Department of Earth Sciences, University of Minnesota, Twin Cities, Minneapolis, MN, USA

**Key Points:**
- We investigate solute breakthrough in sparse three-dimensional discrete fracture networks
- The network structure plays a key role in controlling velocity transitions along a particle pathline
- We uncover a link between structural properties of the network and observed hydrodynamic behavior

**Correspondence to:**
J. Hyman,
jhyman@lanl.gov

**Citation:**
Hyman, J. D., Dentz, M., Hagberg, A., & Kang, P. K. (2019). Linking structural and transport properties in three-dimensional fracture networks. *Journal of Geophysical Research: Solid Earth*, *124*, 1185–1204. https://doi.org/10.1029/2018JB016553

Received 14 AUG 2018
Accepted 15 JAN 2019
Accepted article online 17 JAN 2019
Published online 8 FEB 2019

**Abstract** We investigate large-scale particle motion and solute breakthrough in sparse three-dimensional discrete fracture networks characterized by power law distributed fracture lengths. The three networks we consider have the same fracture intensity values but exhibit different percolation densities, geometric properties, and topological structures. We considered two different average transport models to predict solute breakthrough, a streamtube model and a Bernoulli continuous time random walk model, both of which provide insights into the flow fields within the networks. The streamtube model provides acceptable predictions at short distances in two of the networks but fails in all cases to predict breakthrough times at the outlet plane, which indicates that particle motion in such fracture networks cannot be characterized by a constant velocity between the inlet and control plane at which the breakthrough curve is detected. Rather, the structure of the network requires that frequent velocity transitions be made as particles move through the system. Despite the relatively broad distribution of fracture radii and relatively small number of independent velocity transitions, the continuous time random walk approach conditioned on the initial velocity distribution provides reasonable predictions for the breakthrough curves at different distances from the inlet. The application of these averaged transport models provides a richer understanding of the link from the fracture network structure to flow and transport properties.

## 1. Introduction

Geological structures significantly influence hydrodynamic flows in low-permeability fractured media. Within an isolated fracture, the nonuniform resistance offered by uneven fracture walls leads to irregularities in the flow, the magnitude of which depends on the roughness in the fracture's aperture (Cardenas et al., 2007; de Dreuzy et al., 2012; Fiori & Becker, 2015; Johnson et al., 2006; Kang et al., 2016; Keller et al., 1999, 1995) and the Reynolds number of the flow (Cardenas et al., 2009; Zou et al., 2017). In a fracture network, larger features can play a more dominant role than in-fracture aperture variability in determining the structure of the fluid velocity field (Bisdom et al., 2016; de Dreuzy et al., 2012; Karra et al., 2015; Makedonska et al., 2016). While it is understood that macroscale network traits influence the arrangement of the fluid flow field within a fracture network (Edery et al., 2016; Hyman & Jiménez-Martínez, 2018), a direct link between geometric and topological properties of the fracture network and upscaled transport observables is still lacking. With such a wide range of relevant length scales, several orders of magnitude (Bonnet et al., 2001; Davy et al., 2013; Hardebol et al., 2015), it is challenging to identify which features of a fracture network influence which flow and transport properties. However, characterizing how the structure of a fracture network influences transport behavior therein is critical for many civil and industrial engineering applications such as $CO_2$ sequestration (Jenkins et al., 2015), aquifer storage and management (National Research Council, 1996; Neuman, 2005), environmental restoration of contaminated fractured media (Kueper & McWhorter, 1991; VanderKwaak & Sudicky, 1996), hydrocarbon extraction from unconventional shale aquifers (Hyman et al., 2016; Middleton et al., 2015), and the long-term storage of spent nuclear fuel (Follin et al., 2014; Selroos et al., 2002).

The effects of these multiple scales on the fluid velocity field within the fracture network are borne witness in the breakthrough curves (BTCs) of dissolved chemicals transported by the flow. For example, fluid flow channeling, where a majority of flow occurs in a subregion of the domain, is well documented in both

field experiments (Abelin et al., 1985, 1991; Rasmuson & Neretnieks, 1986) and in numerical simulations (de Dreuzy et al., 2012; Frampton & Cvetkovic, 2011; Hyman et al., 2015; Maillot et al., 2016). Transport in fractured media commonly exhibits non-Gaussian (anomalous) behavior. In particular, power law scaling in the tail of the transport BTCs through fractured media has been observed in field experiments (Becker & Shapiro, 2000, 2003; Gouze et al., 2008; Hadermann & Heer, 1996; Kang et al., 2015) as well as field-scale numerical simulations (Di Donato et al., 2003; Frampton & Cvetkovic, 2007, 2009; Hyman et al., 2015, 2016; Makedonska et al., 2016; Painter et al., 2002). Various models have been proposed to aid in the interpretation of solute breakthrough in fractured media when the advection-dispersion equation fails to provide adequate predictions including the following: the stochastic convective streamtube model (Becker & Shapiro, 2003), continuous time random walk, fractional advection-dispersion equations (Benson et al., 2000a, 2000b), tempered one-sided stable distribution (Cvetkovic, 2011), and multirate mass transfer (Haggerty & Gorelick, 1995). While these models can be calibrated to provide good agreement with data, their parameterizations often lack a direct connection between the properties of the porous media and observed flow and transport properties (Neuman & Tartakovsky, 2009).

Through direct numerical simulation of flow and transport through fracture networks, we uncover a direct link between network structural properties, for example, fracture connectivity, and flow and particle transport behavior. We consider the steady state flow of an isothermal single phase liquid through sparse three-dimensional fracture networks in a 1-km domain. Fracture lengths of the networks follow a power law distribution, which is a property that is commonly observed in the field (Bonnet et al., 2001). Three networks are constructed to have the same fracture intensity (surface area per unit volume) values but different network connectivity structures, that is, network topology, due to different exponents in the power law distribution of fracture lengths. Focusing on the macroscale network structure, we quantify the differences in fracture geometric, for example, size and aperture, and topological, for example, connectivity and position in the network relative to inflow and outflow boundaries, properties between the networks using a graph-based approach (Hyman et al., 2017). Flow and transport through the networks is interpreted using a stochastic convective streamtube model and a Bernoulli continuous time random walk model (Dentz et al., 2016), both of which provide insights into the link between fracture structure and transport properties.

## 2. Flow and Transport Simulations

We consider flow and transport in three synthetic three-dimensional fracture networks that we model using a discrete fracture network (DFN) approach. The choice to use DFNs, rather than stochastic continuum or dual permeability/porosity models, is based on our goal of linking network structure properties to flow observables. DFN models explicitly represent fractures as discrete entities that form a network. While this conceptual formulation of fractured media allows for detailed information about fracture geometry and network topology to be quantified, the computational burdens associated performing direct numerical simulations on large-scale, thousands of individual fractures, three-dimensional DFN are demanding and until recently were prohibitive. Thus, early DFN models used pipe-network approximations (Cacas et al., 1990; Dershowitz & Fidelibus, 1999; Nordqvist et al., 1992) or were two-dimensional models (Berkowitz & Scher, 1997b, 1998; de Dreuzy et al., 2004, 2001, 2002) or modest-sized three-dimensional networks (Andersson & Dverstorp, 1987; Huseby et al., 2001; Long et al., 1982). Nonetheless, these simulations helped develop a better understanding of how fracture and network attributes, such as the distribution of fracture lengths; internal heterogeneity; and variable density, influence flow properties such as effective permeability (Bogdanov et al., 2007; Hamzehpour et al., 2009; Koudina et al., 1998; Mourzenko et al., 2004, 2011). However, recent advances in numerical methods for DFN modeling and evolving high-performance computing (HPC) capabilities have allowed for a resurgence in DFN modeling where flow and transport through larger and more complicated networks, tens of thousands of fractures, can now be simulated, (Berrone et al., 2015; Bonneau et al., 2016; Cacas et al., 1990; Davy et al., 2013; de Dreuzy et al., 2012; Erhel et al., 2009; Hyman et al., 2014, 2015; Joyce et al., 2014; Lang et al., 2014; Maillot et al., 2016; Makedonska et al., 2016).

### 2.1. DFN Simulation

We use the DFNWORKS (Hyman et al., 2015) suite to generate each DFN, solve the steady state flow equations, and determine transport properties therein. DFNWORKS combines the feature rejection algorithm for meshing (FRAM; Hyman et al., 2014), the LaGriT meshing toolbox (LaGriT, 2013), the parallelized subsurface flow and reactive transport code PFLOTRAN (Lichtner et al., 2015), and an extension of the WALKABOUT particle

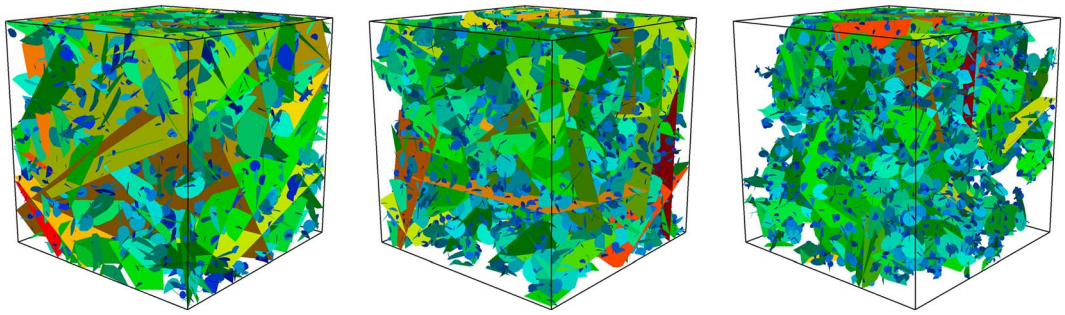

**Figure 1.** Images of the discrete fracture networks that we consider, network 1 (left), network 2 (middle), and network 3 (right). Fractures in the networks all follow a power law distribution (equation (1)) with exponent $\alpha$ of 1.6 (left) 2.2 (middle), and 2.6 (right). Fractures are colored according to their size with warm colors indicating larger fractures. Although the networks have similar fracture intensity, they have vastly different topological structures as well as range of relevant length scales.

tracking method (Makedonska et al., 2015; Painter et al., 2012). FRAM is used to generate three-dimensional fracture networks. LaGriT is used to create a computational mesh representation of the DFN in parallel. PFLOTRAN is used to numerically integrate the governing flow equations. WALKABOUT is used to determine pathlines through the DFN and simulate solute transport. Details of the suite, its abilities, applications, and references for detailed implementation are provided in Hyman et al. (2015).

Three synthetic aperiodic DFN composed of disk-shaped fractures are generated within a cubic domain. Fracture centers are uniformly distributed throughout the domain, and orientations are also uniformly random.

The fracture radii $r$ are sampled from a truncated power law distribution with upper and lower cutoffs ($r_u$; $r_0$) and exponent $\alpha$. The probability density function (PDF) for the radius is given by the following:

$$p_r(r) = \frac{\alpha}{r_0} \frac{(r/r_0)^{-1-\alpha}}{1-(r_u/r_0)^{-\alpha}}. \tag{1}$$

We consider three different values for the power law exponent $\alpha$: 1.6, 2.2, and 2.6. These selected values for the exponent are within the range of values observed in the field (Bonnet et al., 2001). We refer to these networks as network 1 ($\alpha = 1.6$), network 2 ($\alpha = 2.2$), and network 3 ($\alpha = 2.6$). Images of the three networks are provided in Figure 1; network 1 (left), network 2 (middle), and network 3 (right). Fractures are colored according to their size with warm colors indicating larger fractures.

Fracture apertures are determined by correlating their width to the fracture radii using a positively correlated power law relationship:

$$b = \gamma r^{\beta}, \tag{2}$$

where $\gamma = 5.0 \times 10^{-4}$ and $\beta = 0.5$ are dimensionless parameters. This correlation between fracture size and aperture is a common assumption in DFN models (Bogdanov et al., 2007; de Dreuzy et al., 2002; Hyman et al., 2016; Frampton & Cvetkovic, 2010; Joyce et al., 2014; Wellman et al., 2009).

We work in nondimensional variables. Length scales are nondimensionalized by the minimum fracture size $r_0$; $r_0 = r_0/r_0 = 1$, $r_u = r_u/r_0 = 100$, and the domain size is $L = 100r_0$. The distributions of fracture radii are shown in Figure 2 (left) where circles represent network 1, triangles network 2, and diamonds network 3. The reported values show that as $\alpha$ increases, there are fewer large fractures in the networks, a trait that can also be observed in Figure 1.

The requested number of fractures in the networks is selected so that when isolated fractures are removed, the dimensionless fracture intensity $P_{32}r_0$ (network surface area over total domain volume) of the networks are all close to 0.4. While the networks have similar final intensities, they have different densities. We measure the density of the networks using the percolation parameter $p$ defined by De Dreuzy et al. (2000). We use a dimensionless version of $p^* = p/p_c$, where $p_c$ is the critical percolation density value, which is the density the critical density $p_c$ of fractures such that if the density of the network $p < p_c$, then the system is on average not connected, and if $p > p_c$, then the system is connected by a cluster than spans the whole domain; that is, it forms an infinite cluster (Berkowitz & Balberg, 1993; Bour & Davy, 1997, 1998; Sahimi, 1994).

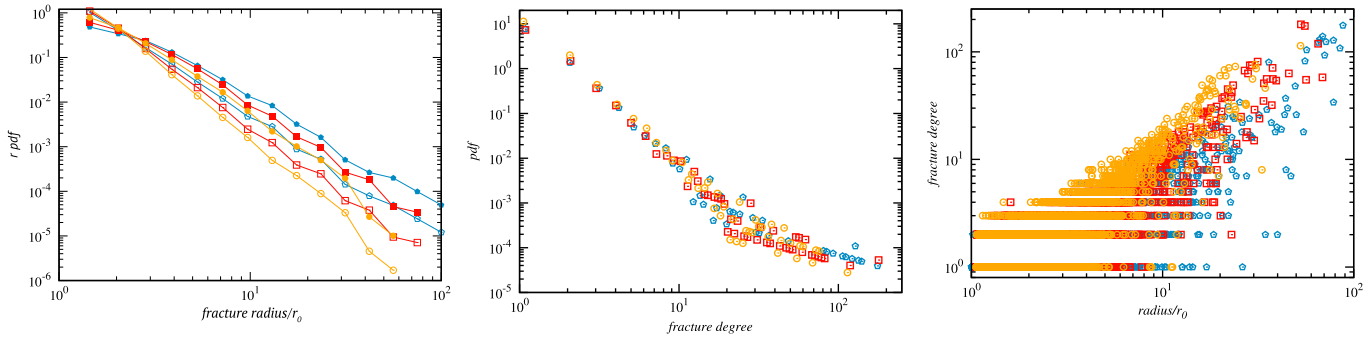


**Figure 2.** (left) Distribution of the fracture radii for the three networks under consideration, which are characterized by the fracture length distribution (1). The blue diamonds represent network 1, the red squares represent network 2, and the orange circles represent network 3. Empty marker are the originally sampled distribution, and filled markers are the final distribution, once isolated fractures and clusters are removed. The networks 1 and 2 have substantially more large fractures than network 3. (middle) Fracture degree distribution. The degree of a fracture is number of other fractures that it intersects, that is, the degree of the corresponding node in the graph representation. The networks exhibit the same behavior for small degrees but differ at higher values. In particular, networks 1 and 2 have more fractures with higher degree; that is, there are more fractures that intersect many other fractures. (right) Plot of fracture degree plotted as a function of fracture radii. In general, small fractures intersect fewer fractures than larger ones.

An advantage of $p^*$ is that it provides a constant measure of density with respect to the percolation threshold regardless of the exponent in the power law distribution (de Dreuzy et al., 2012). Values of $p^*$ are reported in Table 1, and all values are much greater than the percolation threshold, which ensures that there are paths from inflow to outflow boundaries. Note that the domain size, minimum, and maximum fracture size are all fixed so these values highlight how the exponent of the power law plays a key role in determining density relative to the percolation threshold. In case of the network 1, there are the fewest number of fractures in the domain, both prior and after isolated clusters are removed, but the value of $p^*$ is the highest because there is high probability for long fractures that connect across the domain to be sampled and included into the domain, compare circles in Figure 2 (left). Conversely, in the case of network 3, where there are the largest number of fractures, again both prior and after isolated clusters are removed, the value of $p^*$ is the lowest because there is low probability for long fractures to connect across the domain, compare diamonds in Figure 2 (left).

Another result of the different choices of exponent in the power law distribution is that the networks have different topological properties. We characterize and query the topology of each network by representing each network as a graph using the method described in Hyman et al. (2017); details provided in Appendix C. In this particular graph representation, vertices correspond to fractures in the DFN and there is an edge between vertices if the corresponding fractures intersect in the DFN, which is similar to the graph representation of a DFN proposed by Huseby et al. (1997). However, the method is distinguished by the inclusion of source and target vertices, corresponding to the inflow and outflow boundaries, into the graph to provide a topological point of reference with respect to inflow and outflow boundaries. For every fracture that intersects the inflow boundary an edge is added between the vertex in the graph corresponding to that fracture and the vertex representing the inflow boundary; likewise for the outflow boundary. Similar graph theoretical approaches have been used for a variety of studies concerning DFN including topological characterization (Andresen et al., 2013; Huseby et al., 1997; Hope et al., 2015; Hyman & Jiménez-Martínez, 2018) and backbone identification (Hyman et al., 2018; Valera et al., 2018). The utility

**Table 1**
*Network Characterization: Power Law Exponent α, Number of Fractures (# F), Nonisolated Fractures (# $\hat{F}$), Dimensionless Connected Network Density $p^*$, Initial $P_{32}$ [−]), Final $\hat{P}_{32}$ [−]), Dimensionless Mean Radius [−] ($\bar{r}$), Dimensionless Minimum Radius [−] ($r_{\min}$), Dimensionless Maximum Radius [−] ($r_{\max}$), Assortativity Coefficient $\mathcal{P}$, and Number of Vertices in the Shortest Path Between the Inflow and Outflow Boundaries*

| Network | $\alpha$ | # F | # $\hat{F}$ | $p^*$ | $P_{32}$ | $\hat{P}_{32}$ | $\bar{r}$ | $r_{\min}$ | $r_{\max}$ | $\mathcal{P}$ | SPL |
|---|---|---|---|---|---|---|---|---|---|---|---|
| 1 | 1.6 | 13,183 | 3,222 | 93 | 0.60 | 0.42 | 3.9 | 1.0 | 87.9 | −0.20 | 1 |
| 2 | 2.2 | 22,480 | 4,697 | 23 | 0.70 | 0.41 | 3.6 | 1.0 | 68.6 | −0.13 | 2 |
| 3 | 2.6 | 41,752 | 7,055 | 14 | 0.90 | 0.37 | 2.4 | 1.0 | 52.6 | −0.16 | 11 |

of a graph theoretical approach is that topological properties of the networks can be queried and characterized in a formal mathematical framework. For example, once isolated fractures and clusters are removed, we can identify that each network is composed of a single connected component, similar to the analysis performed by Huseby et al. (1997).

Figure 2 (middle) shows the fracture degree distributions for the three networks. We define the degree of a fracture by the number of other fractures that it intersects, that is, the degree of the corresponding node in the graph. The mean of these distributions is equivalent to the dimensionless density detailed in Mourzenko et al. (2005). Many of the fractures connect to few other fractures, but several of them connect to many fractures. Plotted on log-log axis, we see that all of the networks show a skew distribution of the fracture degree distributions, which indicates scale-free network properties (Albert & Barabási, 2002; Barabási & Albert, 1999). As the exponent of the power law fracture size distribution decreases, the exponent of a power law fit to the degree distribution also decreases due to larger fractures connecting to more other fractures. Figure 2 (right) shows the fracture degree distributions for the three networks plotted as a function of the fracture radius to highlight how fractures are connected to one another. In general, larger fractures have higher degree indicating that they are better connected. These observations suggest that the DFNs can be thought of as a series of hubs (large fractures) connected by paths through (smaller fractures). In network 1 and network 2, there are a few primary hubs so particles can move through the system without having to traverse many small fractures. In the case of network 3, more transitions between fractures need to occur. We also compute a measure of degree mixing using the assortativity coefficient $\mathcal{P}$ (Newman, 2002, 2003) of the three networks. The assortativity coefficient measures whether vertices in a graph connect to other vertices with similar degree. It is quantified using the Pearson correlation coefficient (Newman, 2003), which ranges between $-1$ and 1. Values greater than 0 indicate correlation between vertices of similar degree, while values less than 0 indicate correlation between vertices of different degrees. In all cases, the value is less than 0, which indicates that the networks exhibit disassortative mixing. Physically, this means that fractures with a high degree connect to fractures with low degree. Given the previously discussed relationship between fracture degree and fracture size, the values of $\mathcal{P} < 0$ indicate that larger fractures are connected to numerous small fractures.

Another utility of this particular graph representation is that it allows us to compute the shortest topological paths between the inflow and outflow boundaries using Dijkstra's algorithm (Dijkstra, 1959). The number of vertices in the shortest path through the graph corresponds to the fewest number of fractures a particle would have to move through to exit the system starting from the inlet plane. In network 1 there are 2 fractures that directly connect the inflow and outflow boundaries, 36 paths between the inflow and outflow boundaries contain 2 fractures, and 396 paths that contain 3 fractures. In network 2, no fracture directly connects the inflow and outflow boundaries, but there are 3 paths that contain only 2 fractures, and 55 paths made up of 3 fractures. In network 3, the shortest paths between the inflow and outflow boundaries contain 11 fractures. There are 45 of such paths. These values are copacetic with expectations concluded from analysis of the dimensionless density values $p^*$ reported in Table 1.

The provided geometric, fracture size and network intensity, and topological shortest path length, characterization reveals a few key properties about the networks. First, the source and target are well connected in networks 1 and 2 by a few large fractures. Thus, it is possible for particles pass through the domain while only making a few transitions between fractures. On the other hand, particles in the network 3 must make many transitions between fractures before exiting the domain. Therefore, while the network intensities are similar, $P_{32} \approx 0.04$ for all networks, they are topologically quite different. In the following sections, we characterize how these differences influence transport properties.

### 2.2. Flow

The governing equations for an isothermal, incompressible, Newtonian fluid at steady state within the fracture networks are the Stokes equations:

$$\begin{aligned} \mu \nabla^2 \mathbf{u} - \nabla P &= 0 \\ \nabla \cdot \mathbf{u} &= 0, \end{aligned} \tag{3}$$

where $\mu$ is the fluid viscosity and $\nabla P$ is the pressure gradient. Under the assumption of aperture uniformity, flow through individual fractures is equivalent to flow between two parallel plates and (3) can be integrated

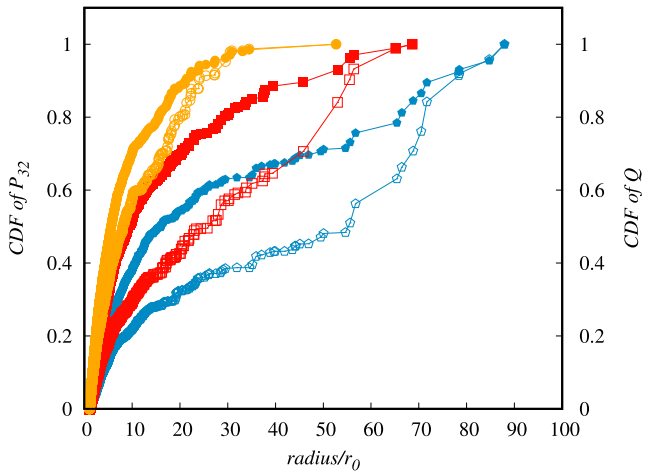


**Figure 3.** Cumulative distribution of surface area (full symbols) and volumetric flow rate (empty symbols) as a function of fracture size for (blue diamonds) network 1, (red squares) network 2, and (orange circles) network 3. CDF = cumulative distribution function.

to determine the volumetric flow rate $Q$ per unit fracture width normal to the direction of flow to obtain

$$\mathbf{Q} = \frac{-b^3}{12\mu}\nabla P, \tag{4}$$

that is, the Boussinesq equation. Note that the relationship between aperture and flow rate can be used to derive a relationship between aperture and transmissivity:

$$T = \frac{b^3}{12}, \tag{5}$$

referred to as the cubic law (Witherspoon et al., 1980). A consequence of (2) and (5) is that fracture's permeability/transmissivity is positively correlated to its size. We assume that the matrix surrounding the fractures is impervious and there is no interaction between flow within the fractures and the solid matrix; matrix diffusion is not considered in these simulations.

We drive flow through the domain by applying a pressure difference of 1 MPa across the domain aligned with the $x$ axis and solving for steady state pressure within the domain. Dirichlet boundary conditions are applied to all nodes in the computation mesh with $x = 0$ and $x = 100r_0$ such that a 1-MPa gradient is formed across the domain. Neumann, no-flow, boundary conditions are applied along lateral boundaries, and gravity is not included in these simulations. These boundary conditions along with mass conservation,

$$\nabla \cdot \mathbf{Q} = 0, \tag{6}$$

are used to form an elliptic partial differential equation for steady state distribution of pressure within each network:

$$\nabla \cdot (b^3 \nabla P) = 0. \tag{7}$$

Once the distribution of pressure and volumetric flow rates are determined by numerically integrating (7), the Eulerian velocity field $\mathbf{u}(\mathbf{x})$ within the DFN is reconstructed from the volumetric fluxes and pressures using the method provided in Makedonska et al. (2015) and Painter et al. (2012). Even though the fracture apertures are uniform within each fracture plane, the in-fracture velocity field is nonuniform. The structure of the flow field within each fractures depends on in-plane boundary conditions, which is determined by the fracture's location within the network.

The differences in power law exponents in the networks control the distribution of fracture surface area in the system, and it also influences the distribution of flow rates in the domain. Figure 3 shows the cumulative distribution function (CDF) of surface area plotted as a function of fracture size. Recall that the $P_{32}$ values are the same for all three networks, so the final surface area is also the same. However, how fractures contribute to these values are quite different in the three networks. Due to the power law distribution of fracture radii, the contribution of each fracture to the cumulative surface area is unbalanced, with a few large fractures contributing the most to the total surface area of the system. This feature is most pronounced in network 1 and network 2. In network 3, the contribution of total surface area is more uniform, due to the narrower range of fracture radius. Along with the surface area is the CDF of volumetric flow rate $Q$, also plotted as a function of fracture radius. In comparison with the CDF of surface area, the jumps in the CDF of $Q$ are even more pronounced and indicate strongly channelized flow. There are a few large fractures that carry a disproportionately large amount of flow relative to their size, most notably in networks 1 and 2. In the case of network 3, the contribution of flow on the majority of fractures is closer to being proportional to their size.

### 2.3. Particle Tracking

We consider here purely advective transport and represent the spreading of a nonreactive conservative solute in the DFN by a cloud of passive tracer particles, that is, using a Lagrangian approach. For the use of particle tracking to solve transport in fracture networks, see also Berkowitz and Scher (1997b) and Huseby et al.

(2001) and the review by Noetinger et al. (2016). The imposed pressure gradient is aligned with the $x$ axis, and thus, the primary direction of flow is also in this direction. Particles are injected over a plane $\Omega_a$ located at $x = 0$ perpendicular to the mean flow direction. Thus, the initial particle positions are $\mathbf{a} = (0, a_2, a_3)^\top$ where the superscript $\top$ denotes the transpose. The area $A$ of the inlet plane is

$$A = \int_{\Omega_a} \mathrm{d}f. \tag{8}$$

The total flux $Q$ over the inlet plane is

$$Q = \int_{\Omega_a} \mathrm{d}\mathbf{a} u(\mathbf{a}), \qquad u(\mathbf{a}) = |\mathbf{u}(\mathbf{a})|, \tag{9}$$

while the total mass injected over the plane is

$$M = \int_{\Omega_a} \mathrm{d}\mathbf{a} m(\mathbf{a}), \tag{10}$$

where $m(\mathbf{a})$ is the areal mass density.

We consider a flux-weighted injection mode that accounts for both aperture and volumetric flow rate where the mass distribution at the inlet is

$$m(\mathbf{a}) = M\frac{u(\mathbf{a})}{Q}. \tag{11}$$

The trajectory $\mathbf{x}(t;\mathbf{a})$ of a particle starting at $\mathbf{a}$ at time $t = 0$ is given by the advection equation:

$$\frac{\mathrm{d}\mathbf{x}(t;\mathbf{a})}{\mathrm{d}t} = \mathbf{v}_t(t;\mathbf{a}), \qquad \mathbf{x}(0;\mathbf{a}) = \mathbf{a}, \tag{12}$$

where the Langrangian velocity $\mathbf{v}_t(t;\mathbf{a})$ is given in terms of the Eulerian velocity $\mathbf{u}(\mathbf{x})$ as

$$\mathbf{v}_t(t;\mathbf{a}) = \mathbf{u}[\mathbf{x}(t;\mathbf{a})]. \tag{13}$$

At fracture intersections, we apply complete mixing such that the probability to enter an outgoing fracture is weighted by its flux. The length $\ell(t;\mathbf{a})$ of the trajectory at a time $t$ is given by

$$\frac{\mathrm{d}\ell(t;\mathbf{a})}{\mathrm{d}t} = v_t(t,\mathbf{a}), \tag{14}$$

where the Lagrangian velocity magnitude is $v_t(t,\mathbf{a}) = |\mathbf{v}_t(t,\mathbf{a})|$. The length of the pathline, $\ell$, is used to parameterize the spatial and temporal coordinates of the particle. The space-time particle trajectory is given in terms of $\ell$ by

$$\frac{\mathrm{d}\mathbf{x}(\ell;\mathbf{a})}{\mathrm{d}\ell} = \frac{\mathbf{v}_\ell(\ell;\mathbf{a})}{v_\ell(\ell;\mathbf{a})} \tag{15a}$$

$$\frac{\mathrm{d}t(\ell;\mathbf{a})}{\mathrm{d}\ell} = \frac{1}{v_\ell(\ell,\mathbf{a})} \tag{15b}$$

where we defined the space-Lagrangian velocity $\mathbf{v}_\ell(\ell,\mathbf{a}) = \mathbf{v}[\mathbf{x}(\ell;\mathbf{a})]$ and its magnitude $v_\ell(\ell,\mathbf{a}) = |\mathbf{v}_\ell(\ell,\mathbf{a})|$.

The first arrival time $\tau(x_1;\mathbf{a})$ of a particle at a control plane located at $x$ is given by

$$\tau(x_1;\mathbf{a}) = t[\lambda(x_1);\mathbf{a}], \qquad \lambda(x_1) = \inf\{\ell | x_1(\ell;\mathbf{a}) \geq x_1\}. \tag{16}$$

The mass represented by each particle and the breakthrough time at each control plane can be combined to compute the complement of the total solute mass flux $F(t,z)$ that has broken through at a time $t$:

$$F(t,x_1) = \frac{1}{M}\int_{\Omega_a} \mathrm{d}\mathbf{a} m(\mathbf{a}) H[\tau(x_1,\mathbf{a}) - t]. \tag{17}$$

Here, $H(t)$ is the Heavyside function where $H(t) = 1$ for $t > 0$, and $H(t) = 0$ otherwise. Equation (17) is the integral form of the complementary CDF of solute passing through a control plane. We refer to $F(t,x)$ as the BTC. To generate the BTCs, one million particles are tracked through each network. Detailed Lagrangian information, for example, the stationary space Lagrangian velocity PDF, are obtained using 100,000 particles

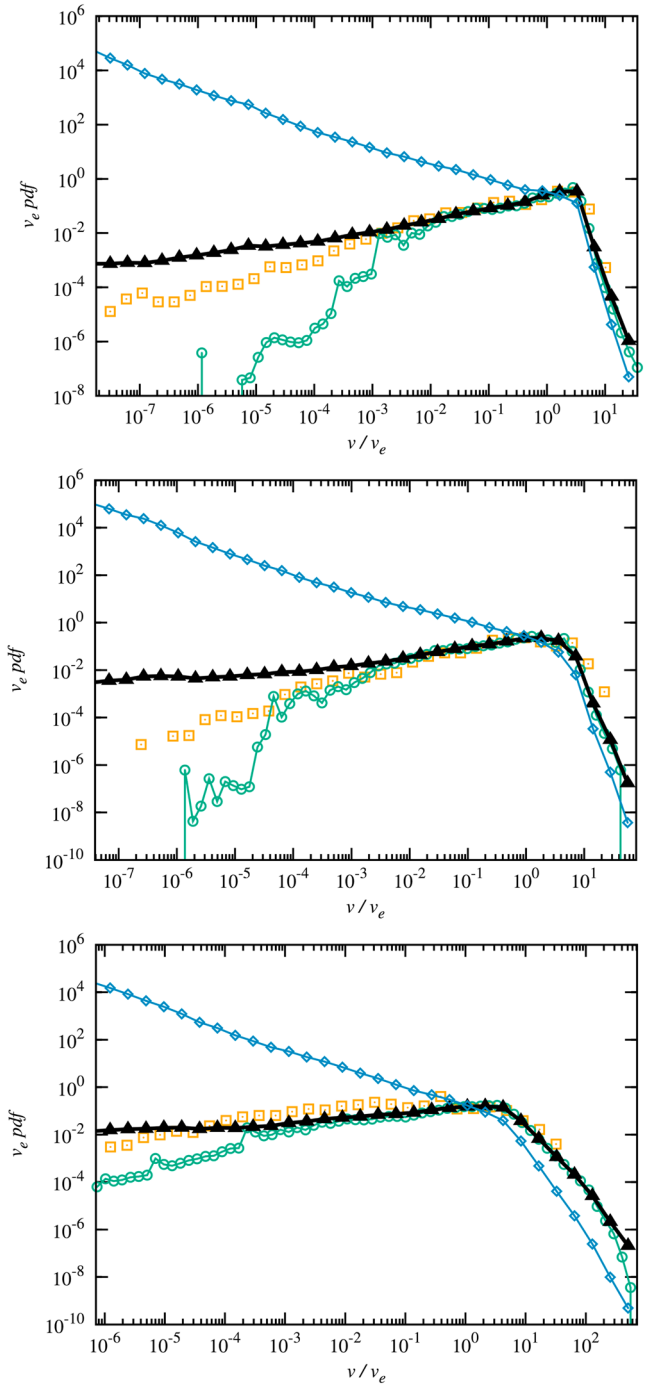


**Figure 4.** (circles) Stationary space Lagrangian velocity probability density function (PDF), (squares) spacial sampled velocity PDF at the inlet plane, (diamonds) Eulerian velocity PDF, and (triangles) flux-weighted Eulerian velocity PDF for (top to bottom) networks 1–3.

due to memory and disk space limitations; all Lagrangian information is postprocessed and must be saved. Increasing the number of particles beyond these counts did not influence these upscaled quantities.

## 3. Flow and Transport Behavior

In this section, we analyze the flow behavior in terms of distribution of the Eulerian velocity magnitude. Particle transport is characterized by the tortuosity of particle pathlines and particle arrival times at different distances from the inlet plane. The breakthrough behavior is compared to a simple prediction based on a stochastic convective streamtube approach. This approach has been used for the prediction of transport in highly heterogeneous fractured (Becker & Shapiro, 2003) and porous media (Cirpka & Kitanidis, 2000; Dagan & Bressler, 1979; Ginn et al., 1995). It assumes that particle velocities along pathlines are approximately constant and transport is dominated by velocity contrast between streamtubes. We expect this approach to hold relatively close to the inlet plane.

### 3.1. Velocity Distributions

The PDF of the Eulerian velocity magnitude $v_e(\mathbf{x}) = \|\mathbf{u}(\mathbf{x})\|$ is given by

$$p_e(v) = \frac{1}{V_e}\int_{\Omega_e} \mathrm{d}\mathbf{x}\delta[v - v_e(\mathbf{x})], \tag{18}$$

where $\Omega_e$ is the flow domain and $V_e$ its volume. The PDF of the space Lagrangian velocity magnitude $v_\ell(\ell)$ is given by

$$\hat{p}_\ell(v,\ell) = \frac{1}{M}\int_{\Omega_a} \mathrm{d}\mathbf{a}m(\mathbf{a})\delta[v - v_\ell(\ell,\mathbf{a})]. \tag{19}$$

Under ergodic conditions, this means for a sufficiently large injection volume and flow domain, the steady space Lagrangian PDF $p_\ell(v) = \lim_{\ell\to\infty}\hat{p}_\ell(v,\ell)$ and the Eulerian velocity PDFs are related through flux-weighting as shown in (Comolli & Dentz, 2017; Dentz et al., 2016; Kang et al., 2017):

$$p_\ell(v) = \frac{vp_e(v)}{\langle v_e\rangle}. \tag{20}$$

Computationally, the PDFs of Eulerian velocity magnitude are directly obtained from the reconstructed $\|\mathbf{u}(\mathbf{x})\|$ velocity field and the Lagrangian PDFs are obtained using the particle tracking methods described above.

The PDF of velocity magnitudes in the injection domain is given by $p_0(v) = \hat{p}_\ell(v,\ell = 0)$. Figure 4 shows the Eulerian, flux-weighted Eulerian, and the space Lagrangian velocity PDFs as well as the space Lagrangian velocity PDF at the injection plane for the three fracture networks under consideration. First, the maximum Eulerian velocities and the Eulerian average velocities decrease with decreasing power law exponent $\alpha$. This observation is related to positive correlation of aperture with the fracture lengths, the later decreases with increasing $\alpha$ (cf. Table 1). Second, we observe that the distribution $p_0(v)$ of velocity magnitudes at the inlet plane and $p_\ell(v)$ are in good agreement at high velocities, while they deviate toward low velocities. For network 1 they start deviating at around $v/v_e = 10^{-3}$, for network 2 at around $v/v_e = 10^{-5}$ and for network 3 they stay at the same order of magnitude until around $v/v_e = 10^{-6}$. This behavior can be traced back to the fact that, for the same cross-sectional area, the velocity variability in a cross section is higher for a dense than a sparse network, and closer to the overall variability sampled throughout the medium. These features can also be observed by comparing the flux-weighted Eulerian and space Lagrangian velocity PDFs. According to relation (20), they are equal under ergodic conditions. Both PDFs coincide well at high velocity magnitudes and start deviating at low velocities. Specifically, for network 1, both PDFs compare well to velocities of around $v = 10^{-3}$, for network

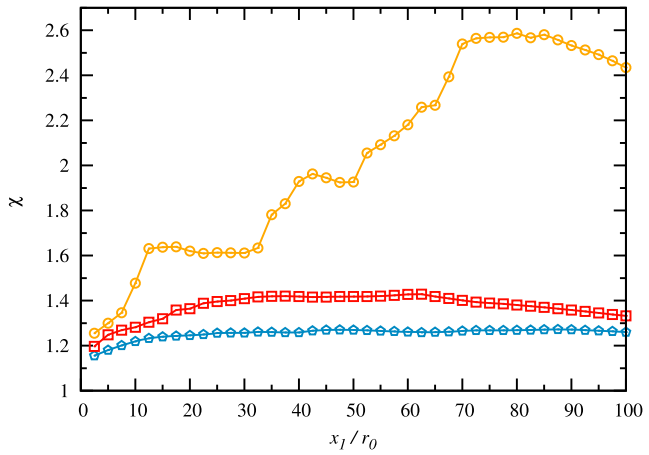


**Figure 5.** Mean tortuosity as a function of distance $x_1$ traveled for network 1 (blue diamonds), network 2 (red squares), and network 3 (orange circles).

2 down to $\nu = 10^{-2}$, and for network 3 until $10^{-3}$. This behavior can also be attributed to the finite flow domain and the number of fractures in the flow domain which is $\#F = 3,222$ for network 1, 4,697 for network 2, and 7,055 for network 3 (cf. Table 1).

### 3.2. Tortuosity

The length of a particle path when a particle first arrives at a linear distance $x_1$ is given by $\lambda(x_1)$ in (16). The length of the pathline is in general larger than the linear distance. This notion is quantified by tortuosity:

$$\chi(x_1) = \frac{\langle \lambda(x_1) \rangle}{x_1} \tag{21}$$

which measures the ratio between the average path length and linear distance. Under ergodic conditions, this means here at a linear distance $x_1 \gg \ell_c$ much larger than the characteristic fracture length, the tortuosity is given by (Koponen et al., 1996)

$$\chi_\infty = \lim_{x_1 \to \infty} \chi(x_1) = \frac{\langle v_e \rangle}{\langle u_1 \rangle}. \tag{22}$$

The asymptotic tortuosity is highest for the network 3, namely, $\chi_\infty = 2.71$ because the higher number of relatively short fractures induces a high tortuosity in the particle path. For networks 1 and 2, the average fracture length increases; as a result, particle paths are less tortuous with $\chi_\infty = 1.36$ for network 1 and $\chi_\infty = 1.47$ for network 2.

At finite distances $x_1$, however, the tortuosity depends on the local geometry and fluctuates as illustrated in Figure 5. For all three networks, the tortuosity at short distances is low because particles move predominantly through single fractures. As particles start sampling different fractures and path lines change orientation, the tortuosity increases. The strongest increase can be observed in network 3, which has the highest directional disorder. Note that, in this case, the shortest path connecting the inflow and outflow boundary contains 11 fractures. For the networks 1 and 2 there are two fractures directly connecting the inflow and outlet boundaries, while in network 2 there two paths that connect via two fractures. As a consequence of these features, the observed values of tortuosity do not reach the corresponding asymptotic value $\chi_\infty$ in any of the three networks, but they are not far from these asymptotic values.

### 3.3. BTCs

We consider here particle BTCs for the three different networks. Figure 6 shows the BTCs for networks 1–3 at control planes located at dimensionless distances of $x_1 = 25, 50$, and $100r_0$. Time is rescaled by $\tau_v = r_0/\langle v_e \rangle$, distances by $r_0$. The solution for the BTC $F(t, x_1)$ of an equivalent advection-dispersion equation characterized by a constant effective velocity $v_{eff}$ and macrodispersion coefficient $D_m$ is given by Kreft and Zuber (1978):

$$F(t,x_1) = 1 - \frac{1}{2}\left[\operatorname{erfc}\left(\frac{x_1 - v_{eff}t}{\sqrt{4D_m t}}\right) + \exp\left(\frac{x_1 v_{eff}}{D_m}\right)\operatorname{erfc}\left(\frac{x_1 + v_{eff}t}{\sqrt{4D_m t}}\right)\right]. \tag{23}$$

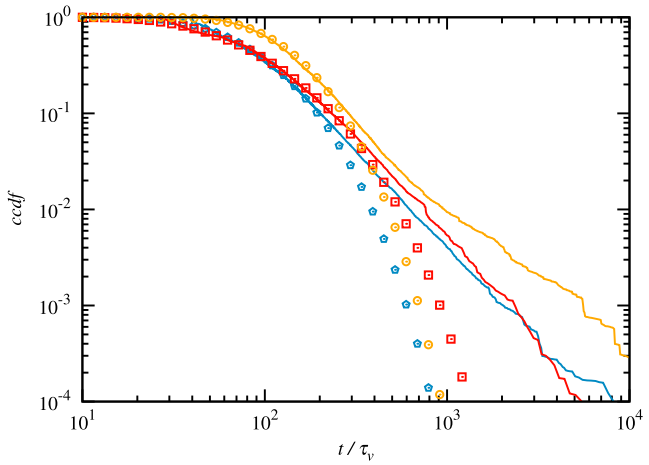


**Figure 6.** Breakthrough curves at $x = 100r_0$ for (blue) network 1, (red) network 2, and (orange) network 3. The solid lines denote the direct numerical simulations, and the symbols denote the corresponding best fit of the solution (23) of an equivalent the advection-dispersion equation. ccdf = complementary cumulative distribution function.

Figure 6 compares the BTC data for $x_1 = 100r_0$ with the best fit of solution (23) with respect to $v_{\text{eff}}$ and $D_m$. The BTCs in all cases show pronounced non-Fickian behavior (power law tailing), which cannot be captured in terms of an equivalent homogeneous porous medium whose transport properties are characterized by macrodispersion. For networks 1 and 2, the first arrival is significantly earlier than for network 3. This can be traced back to the fact that the tortuosity increases as $\alpha$ increases and to the coupling of fracture length and aperture. Networks 1 and 2 have a higher proportion of longer and thus more conductive fractures. The stronger tailing of the BTC for network 3 compared to networks 1 and 2 reflects the higher probability of low velocities; see Figure 4.

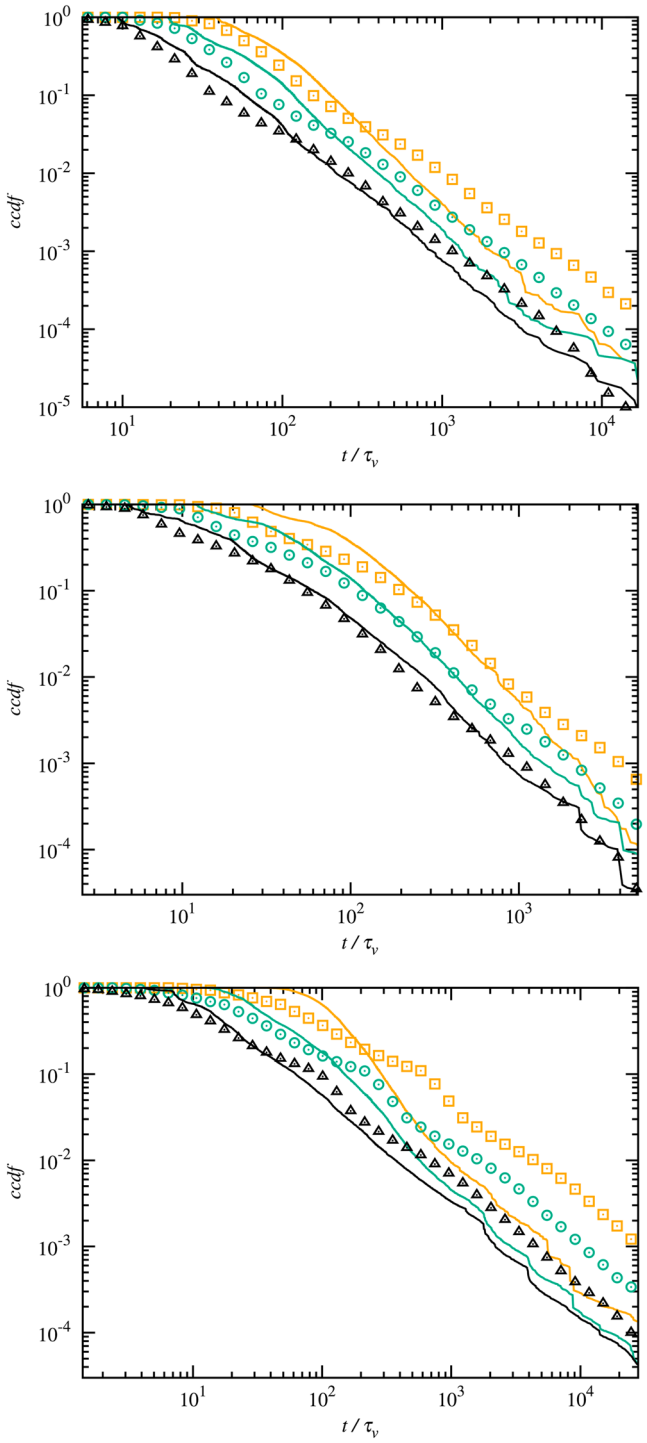


**Figure 7.** Breakthrough curves at (black) $x = 25$, (green) 50, and (orange) $100r_0$ for (top to bottom) networks 1–3. The solid lines denote the direct numerical simulations, and the symbols denote the estimation based on expression (24) obtained from the stochastic convective streamtube approach.

We compare the behavior of the BTCs with the prediction of a stochastic convective streamtube model (Becker & Shapiro, 2003; Kang et al., 2015). This model assumes that transport occurs along streamtubes each of which has a constant velocity $v$. The velocity between streamtubes is distributed according to $p_0(v)$. This assume that particle paths between the inlet and outlet can be characterized by a single constant velocity and thus that the velocity in the fractures sampled along this path are essentially equal. The travel time along a streamtube thus is given by $\tau(x_1, \mathbf{a}) = x_1\chi(x_1)/u(\mathbf{a})$, where $x_1\chi(x_1)$ is the average streamline length between the inlet and control plane. Thus, the solute BTC is given in terms of the velocity PDF as

$$F(t, x_1) = \int_0^{x_1\chi(x_1)/t} \mathrm{d}v' p_0(v'), \tag{24}$$

where $p_0(v)$ is the velocity distribution at the inlet plane discussed in section 3.1 for each network; see Appendix A.

For network 1, the BTCs at $x_1 = 25r_0$ and $x_1 = 50r_0$ are reasonably well predicted by expression (24) with a slight overprediction of the tails; see Figure 7. The estimation based on the stochastic streamtube approach deteriorates at $x_1 = 100r_0$, for which (24) predicts a much stronger tailing than observed from the direct numerical simulations. A similar behavior is observed in network 2 (Figure 7). Here, the BTC is well predicted by expression (24), which indicates that the inlet plane is connected to the detection plane at $x_1 = 25r_0$ by fractures of lengths $\geq 25r_0$. For $x_1 = 50r_0$ and $100r_0$, the stochastic streamtube model predicts too early arrival and overestimates the late time tailing compared to the direct numerical simulations. For network 3 (Figure 7), the stochastic convective streamtube models overestimates tailing of the BTCs at all distances from the inlet. For $x_1 = 25r_0$, the early arrival is predicted reasonably well, while for $x_1 = 50r_0$ and $x_1 = 100r_0$ the streamtube prediction arrives too early and strongly overestimates the late time tailing. These observations indicate that particle motion can in general not be characterized by a constant velocity between the inlet and control plane at which the BTC is detected but is dominated by frequent velocity transitions. In summary, for the shortest distance of $x_1 = 25r_0$, the streamtube prediction performs relatively well with better performance for decreasing $\alpha$ because the average fracture length increases and it is more likely that a fracture connects directly from the inlet to the control plane. It is worth noting as well that the streamtube model provides significantly better predictions that the advection dispersion equation. In the next section, we present a time domain or CTRW framework in order to capture particle motion due to velocity transitions as a result of transitions between fractures.

## 4. Stochastic Particle Motion

In the previous section, we have seen that the particle motion through the fracture network cannot be understood by fully persistent velocities in the framework of a stochastic convective streamtube approach. Instead, particle motion seems to be determined by velocity transitions, which coincide with the particle's transition between fractures. This is illustrated in Figure 8, which shows the velocity variability along a single particle trajectory versus the number of the fracture that it traverses for six particles. Two particles from each network are shown in each column (left: network 1, middle: network 2, and right: network 3). The green line shows the velocity magnitude, and the blue line shows the fracture number on which the particle is currently traveling as a function of pathline

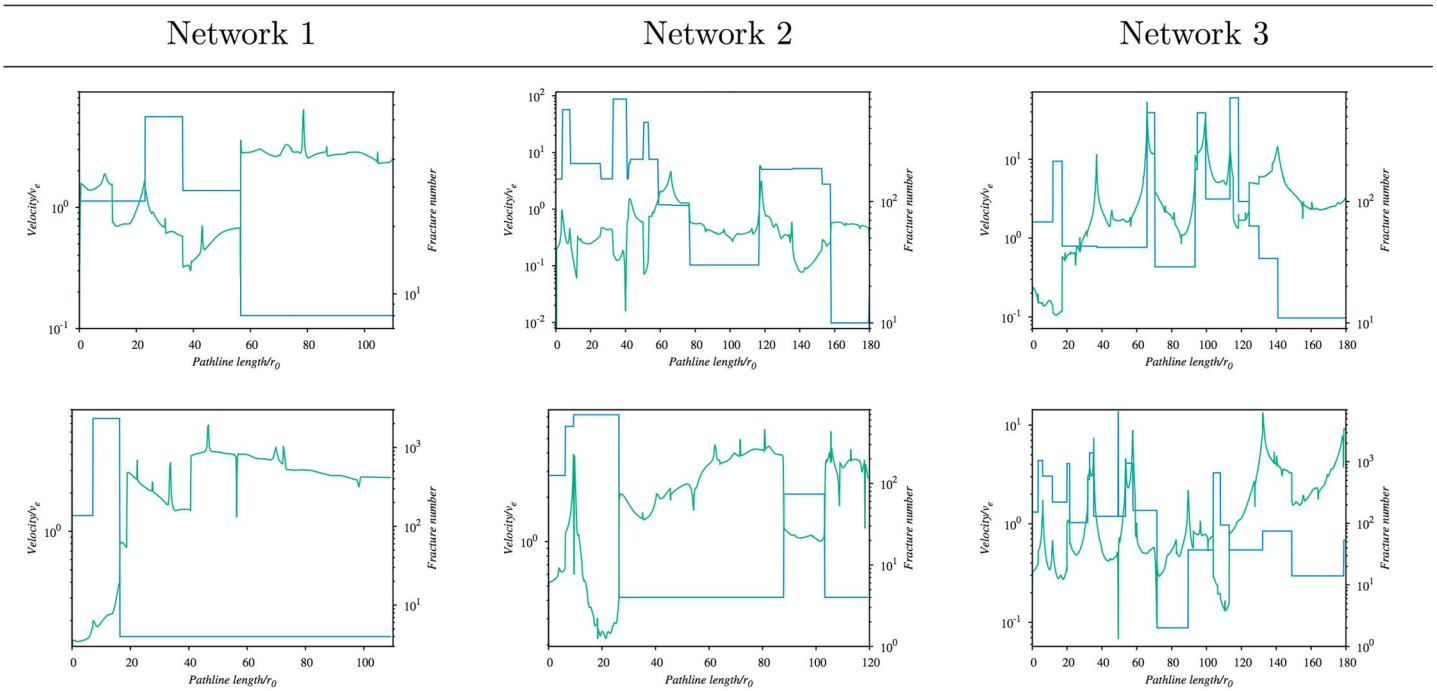


**Figure 8.** Particle velocity changes (green line) and current fracture number (blue line) as a function of pathline length. Two particles from each network are shown in each column (left: network 1, middle: network 2, and right: network 3). Changes in fracture correspond to larger changes in particle velocity. There are more transitions in network 3 than in network 2, and there are more transitions in 2 than network 1.

distance. Note that fractures are numbered in decreasing order based on their radii; that is, the largest fracture is number 1 and smallest of $N$ fractures is number $N$. The velocity variability inside a single fracture is low compared to the variability between fractures; local peaks in the velocity that do not align with changes in the fracture number are the result of a particle passing through a line of intersection but not changing fractures. Particles in network 1 make fewer than in network 2, and network 2 makes substantially fewer transitions than network 3, where transitions are more frequent.

### 4.1. Velocity Correlation

The velocity transition length is determined from the magnitude of particle velocities sampled equidistantly along streamlines as

$$C_{vv}(\ell) = \frac{1}{V_0}\int_{\Omega_0} d\mathbf{a}\int_0^\infty d\ell' \frac{v'_{\ell'}(\ell';\mathbf{a})v'_{\ell'}(\ell'+\ell;\mathbf{a})}{\sigma^2_{vv}}, \tag{25}$$

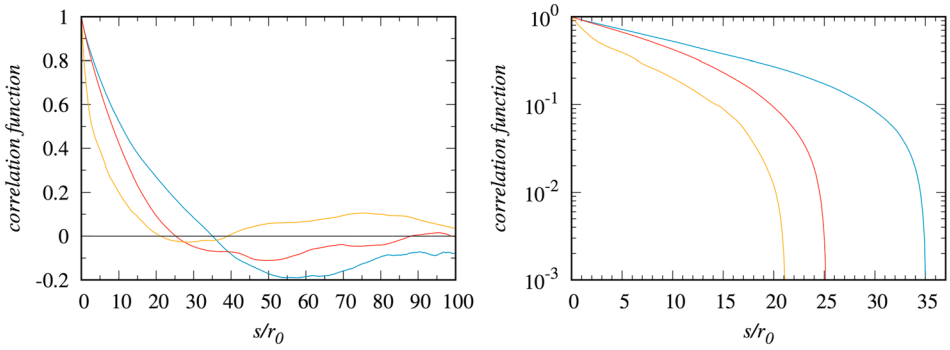


**Figure 9.** Correlation functions of particle velocity magnitude sampled spatially along streamlines for (blue) network 1, (red) network 2, and (orange) network 3. (left) Linear scale and (right) log-linear scale.

where $\sigma^2_{vv}$ is the velocity variance and $v\ell'(\ell;\mathbf{a})$ the fluctuation about the mean. We assume stationarity. Figure 9 shows the correlation functions for the different networks. The correlation distance $\ell_c$ here is defined as the distance at which the velocity fluctuations anticorrelate, which we take at the first zero crossing. Thus, we obtain for network 1 a velocity correlation length $\ell_c = 35r_0$, for network 2, we find $\ell_c = 25.3r_0$, and network 3 the correlation length is $\ell_c = 15r_0$; see Figure 9. Again, we have nondimensionalized the distances by the minimum fracture radius. We define the average number of velocity transitions $n(x_1)$ between the inlet and the detection plane at $x_1$ by the average path length $\chi(x_1)x_1$ divided by the velocity correlation length $\ell_c$ as $n(x_1) = \chi(x_1)x_1/\ell_c$. For network 1, particles perform an average of $n(100r_0) \approx 3.56$ transitions between the inlet and outlet planes, for network 2 it is $n(100r_0) \approx 5.2$, and for network 3 $n(100r_0) \approx 17.33$. Note that the number of transitions is significantly higher for network 3 because the correlation length is shorter and the tortuosity is much higher than for networks 1 and 2; see Figure 5. Notice that the different shortest path lengths of the three different networks (Table 1) is also reflected in the correlation distance and average number of velocity transitions. The variability in the correlation lengths explains the deterioration of the streamtube approach in section 3.3 for increasing values of $\alpha$. In the following, we use a stochastic modeling approach that honors the fact that particles make velocity transitions along pathlines and models them as a simple Bernoulli-type Markov process. This formulation gives rise to a Continuous Time Random Walk type average transport model.

### 4.2. Continuous Time Random Walk

We model effective particle motion by a Continuous Time Random Walk (CTRW), which is characterized by a Bernoulli velocity process that accounts for velocity transitions at a constant spatial rate $\kappa_c = 1/\ell_c$, where $\ell_c$ is the correlation distance. We consider particle motion along pathlines characterized by the constant increment $\Delta\ell \ll \ell_c$. The corresponding transition time for the $n$th step is $\tau_n = \Delta\ell/v_n$, where $v_n$ is the particle velocity magnitude. The velocities are updated according to a Bernoulli process; this means that the velocity remains equal to the velocity at the previous step with probability $p_B = \exp(-\Delta\ell/\ell_c)$ and changes randomly to a velocity sampled from the steady velocity PDF $p_\ell(v)$ with probability $1 - p_B$. In summary, the particle motion is given by (Dentz et al., 2016)

$$\ell_{n+1} = \ell_n + \Delta\ell, \qquad t_{n+1} = t_n + \frac{\Delta\ell}{v_n}, \tag{26a}$$

and the evolution of particle velocities is modeled by

$$v_{n+1} = v_n\xi_n + (1 - \xi_n)v_n, \tag{26b}$$

where $p_\xi(\xi) = p_B\delta(\xi - 1) + (1 - p_B)\delta(\xi)$ and $v$ is distributed according to $p_\ell(v)$. The particle velocities at the first step are drawn from the initial velocity distribution $p_0(v)$. Note that CTRW approaches based on velocity Markov models have been used for the prediction of transport in fractured (Benke & Painter, 2003; Kang et al., 2011) and porous media (Dentz et al., 2016; Le Borgne et al., 2008b, 2008a).

BTCs are recorded at distances $x_1$ from the inlet plane, which corresponds to a path length of $\ell = x_1\chi(x_1)$, where the tortuosity $\chi(x_1)$ is defined by (21). Thus, the particle travel time to a dimensionless distance $\ell$ in this framework is given by

$$t(\ell) = \sum_{n=0}^{n_\ell - 1} \frac{\Delta\ell}{v_n}, \tag{27}$$

where $n_\ell = \lfloor \ell/\Delta\ell \rfloor$ with $\lfloor\cdot\rfloor$ the floor function. The joint PDF of arrival times $t(\ell)$ and particle velocity $v(\ell) = v_{n_\ell}$ is given by

$$f(t, v; \ell) = \langle \delta[t - t(\ell)]\delta[v - v(\ell)] \rangle. \tag{28}$$

It evolves according to the Boltzmann-type equation

$$\frac{\partial f(t, v; \ell)}{\partial t} - v\frac{\partial f(t, v; \ell)}{\partial \ell} = -v\kappa_c f(t, v; \ell) + v\kappa_c p_\ell(v) \int_0^\infty \mathrm{d}v' f(t, v'; \ell). \tag{29}$$

with the initial condition $f(t, v; \ell = 0) = \delta(t)p_0(v)$; see Appendix B and Massoudieh et al. (2017). The arrival time density $f(t; \ell) = \langle \delta[t - t(\ell)] \rangle$ is obtained from $f(t, v; \ell)$ by marginalization:

$$f(t; \ell) = \int_0^\infty \mathrm{d}v f(t, v; \ell). \tag{30}$$

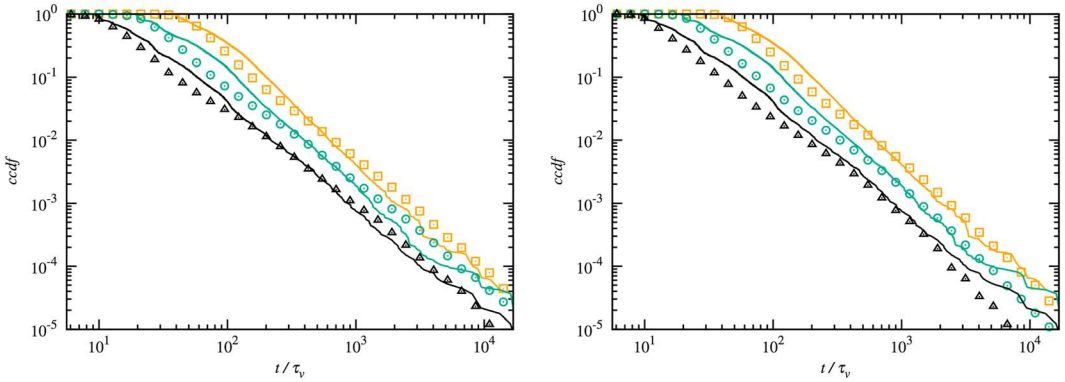


**Figure 10.** Breakthrough curves at $x = 25$, 50, and $100r_0$ for network 1. Direct numerical simulations are lines, and markers correspond to model predictions of the (left) conditional CTRW and (right) steady CTRW with $\Delta\ell = 1$. CTRW = continuous time random walk; ccdf = complementary cumulative distribution function.

The BTC $F(t, x_1)$ is given in terms of $f(t, v; \ell)$ as

$$F(t, x_1) = \int_t^\infty \mathrm{d}t' f[t'; \ell(x_1)]. \tag{31}$$

Note that this approach is based on the knowledge of the distribution of the Eulerian velocity magnitude, a transport independent flow property, the correlation length $\ell_c$, and tortuosity and can be conditioned on the distribution of particle velocities at the inlet and thus on the injection mode. The joint PDF can be written as $f(t, v; \ell) = f(t, \ell|v)p_v(v; \ell)$, where $p_v(v, \ell)$ is the velocity distribution at a distance $\ell$. For the velocity model (26b) it is (Dentz et al., 2016)

$$p_v(v, \ell) = p_\ell(v) + \exp(-\ell/\ell_c)\left[p_0(v) - p_\ell(v)\right]. \tag{32}$$

Under steady conditions, this means for $p_0(v) = p_\ell(v)$ and thus $p_v(v; \ell) = p_\ell(v)$, the evolution equation for the conditional density $f(t, \ell|v)$ is simply

$$\frac{\partial f(t, \ell|v)}{\partial t} - v\frac{\partial f(t, \ell|v)}{\partial \ell} = -v\kappa_c f(t, \ell|v) + v\kappa_c \int_0^\infty \mathrm{d}v' p_\ell(v') f(t, \ell|v'). \tag{33}$$

In the following, we apply the CTRW model (26a) to the breakthrough data from the direct numerical simulations.

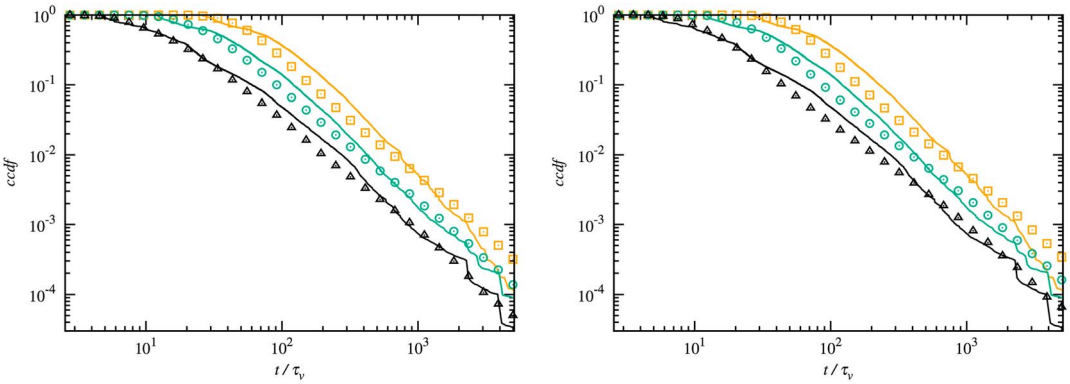


**Figure 11.** Breakthrough curves at $x = 25$, 50 and $100r_0$ for network 2. Direct numerical simulations are lines, and markers correspond to model predictions of the (left) conditional CTRW and (right) steady CTRW with $\Delta\ell = 1$. CTRW = continuous time random walk; ccdf = complementary cumulative distribution function.

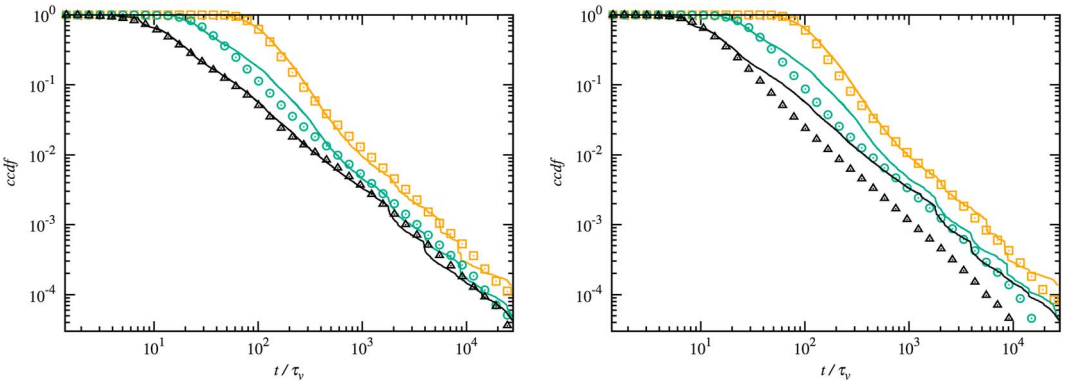


**Figure 12.** Breakthrough curves at $x = 25$, 50, and $100r_0$ for network 3. Direct numerical simulations are lines and markers correspond to model predictions of (left) conditional CTRW and (right) steady CTRW with $\Delta\ell = 1$. ccdf = complementary cumulative distribution function; CTRW = continuous time random walk.

### 4.3. Results

Figures 10–12 show the predictions of the CTRW model presented in the previous section compared to the direct numerical simulations. We consider the CTRW model (26a) conditioned on the initial velocity PDF $p_0(v)$, and for a steady state velocity, this means we set $p_0(v) = p_\ell(v)$. In all cases the CTRW model conditioned on the initial velocity PDF provides a satisfying prediction for the evolution of the breakthrough behaviors with distance from the inlet plane.

Figure 10 shows the CTRW prediction for network 1 compared to the numerical data. Both CTRW models, the one conditioned on the initial velocity data and the steady CTRW model, perform similarly well, while the former predicts better the BTC at distance $x_c = 25r_0$. As we can see in Figure 4, the initial velocity PDF and the steady velocity PDF coincide well down to velocities of $v/v_e = 10^{-3}$. This is sufficient to render similar predictions of the BTCs at different control planes.

This behavior is similar for network 2, as shown in Figure 11. Both the conditional and the steady CTRW models perform equally well because the initial and steady velocity PDFs are very similar; see Figure 4. At the shortest distance of $x_c = 25r_0$, the breakthrough behavior is quite well described by the streamtube model, see Figure 7, better than either of the two CTRW approaches. This indicates that in this network particle transport is dominated by very few long fractures, which is not captured by the CTRW models based on (self-) convolution. However, at long distances ($x_c = 50r_0$ and $x_c = 100r_0$), the streamtube model fails to provide good predictions because particles have made several velocity transitions between fracture planes and the BTC is constructed by convolution. The CTRW model accounts for these transitions and provides better predictions that the streamtube model.

For network 3, there is a remarkable difference between the predictions at $x_c = 25r_0$ based on the conditional and steady CTRW models. The steady CTRW does not capture the breakthrough behavior. This is due to the difference between the initial and steady state velocity PDFs shown in Figure 4. The initial PDF has a higher weight at small velocities, and as a consequence, there is a stronger tailing in the conditioned CTRW and the direct simulations than the predictions provided by the steady CTRW model. At larger distances then, both CTRW models provide good predictions for the direct numerical data.

## 5. Conclusion

We have presented an analysis of flow and transport properties in sparse three-dimensional fracture networks with fracture sizes that follow a power law distribution. The three networks we consider have the same fracture intensity values but exhibit different topological structures, which appear to be the dominant control of transport within the networks, due to the different exponents in the power law distribution of fracture radii. We considered two different average transport models to predict solute breakthrough, a streamtube model and a Bernoulli CTRW model, both of which provide insights into the flow fields within the networks.

The streamtube model provides adequate predictions at short distances in two of the networks but fails in all cases to predict breakthrough times at the outlet plane. The breakdown of the streamtube predictions with increasing distance from the inlet plane indicates that particle motion in such fracture networks cannot be characterized by a constant velocity between the inlet and control plane at which the BTC is detected, as assumed by the streamtube model. Rather, the structure of the network requires that frequent velocity transitions be made as particles move through the system. Despite the relatively broad distribution of fracture radii and relatively small number of independent velocity transitions, the Bernoulli CTRW approach conditioned on the initial velocity distribution and tortuosity of trajectories provides reasonable predictions for the BTCs at different distances from the control because it accounts for these velocity transitions. Through the application of the graph-based characterization method and average transport model interpretation we are able to provide a link between structural properties of the network and observed transport behavior.

For networks 1 and 2 (Figure 7), the streamtube model does a reasonable job predicting breakthrough at detection planes close to the inlet plane but deteriorates when predicting transport at the outlet. These predictions corroborate the notion that the inlet plane is well connected to the early detection planes in these two networks, as identified by the topological investigation in section 2.1. However, for network 3 (Figure 7), the stochastic convective streamtube models overestimates tailing of the BTCs at all distances from the inlet. For $x_1 = 25r_0$, the early arrival is predicted reasonably well, while for $x_1 = 50r_0$ and $x_1 = 100r_0$ the streamtube prediction arrives too early and strongly overestimates the late time tailing. These observations indicate that particle motion can in general not be characterized by a constant velocity between the inlet and control planes at which the BTC is detected. Rather, the structure of the network requires that frequent velocity transitions be made as particles move through the system, as suggested by the preliminary topological investigations. The variability in the correlation lengths explains the deterioration of the streamtube approach in section 3.3 for increasing values of $\alpha$. The shortest path lengths of the networks (Table 1) provide a reasonable starting point for the average number of transitions that particles make (section 4.1); particles in networks with lower shortest path lengths make fewer transitions than particles in networks with longer paths.

The Bernoulli CTRW model accounts for frequency of these transitions and in turn provides better predictions than the streamtube model. We also consider two variants of the model. The first is conditioned on the initial velocity, and the second uses a steady state velocity. In all cases the conditioned CTRW model provides a satisfying prediction for the evolution of the breakthrough behaviors with distance from the inlet plane (Figures 10 –12). Despite the relatively broad distribution of fracture radii and relatively small number of independent velocity transitions, the CTRW approach provides reasonable predictions for the BTCs at different distances from the inlet. We expect the quality of the prediction and the predictability to increase with increasing distance from the inlet plane, as a result of the increasing number of velocity transitions as particles pass through the DFN because they must transition between an increasing number of fractures. This aspect is borne witness by the predictions obtained in network 3, where the highest number of transitions are expected. It is also interesting to note that conditioning on the particle velocities at the inlet plane is most important for network 3 because the difference between the initial velocity distribution and the steady velocity distribution is most pronounced for this network. This emphasizes the importance of conditioning on the initial data. At the distances considered here, the breakthrough behavior is influenced by the local network structure. This nonstationary behavior is captured on one hand by conditioning on the initial velocity PDF and on the other through distance-dependent tortuosity. Typically, this is a parameter that is not easily accessible. However, at large distance, it converges to $\chi_\infty$, which can be determined from the Eulerian flow properties only.

While these networks do present different topological characteristics, it must be noted that they are only three networks with a single fracture intensity. Thus, the presented results are limited in that they provide a first attempt to validate simplified models for flow and transport in complex fracture networks, and further validation is still required. Nonetheless, the success and failure of the models provide insight into the connection between the network structure and the flow properties therein.

## Appendix A: Streamtube Model

The BTC $F(t, x_1)$ is obtained by inserting $\tau(x_1, \mathbf{a}) = x_1 \chi(x_1)/u(\mathbf{a})$ for the arrival time in the streamtube model into expression (17) for the BTCs, which gives

$$F(t, x_1) = \frac{1}{M} \int_{\Omega_a} \mathrm{d}\mathbf{a} m(\mathbf{a}) H[x_1 \chi(x_1)/u(a) - t]. \tag{A1}$$

This expression can be written as

$$F(t, x_1) = \int_0^\infty \mathrm{d}v' H[x_1 \chi(x_1)/v' - t] \left\{ \frac{1}{M} \int_{\Omega_a} \mathrm{d}\mathbf{a} m(\mathbf{a}) \delta[v' - u(\mathbf{a})] \right\}. \tag{A2}$$

We note that the expression in the curly bracket on the right side is equal to the velocity PDF $p_0(v)$ at the inlet. Thus, from (A2) follows immediately (24).

## Appendix B: Boltzmann Equation

The joint PDF (28) of arrival time and velocity can be expanded as

$$f(t, v; \ell + \Delta\ell) = \int_0^\infty \mathrm{d}v' f(t - v'/\Delta\ell, v'; \ell) p_\ell(v, \Delta\ell | v'), \tag{B1}$$

where $p_\ell(v, \Delta\ell | v')$ is the PDF of $v(\ell + \Delta\ell)$ given that is it equal to $v'$ at $\ell$. For the Bernoulli velocity model it is (Dentz et al., 2016)

$$p_\ell(v, \Delta\ell | v') = \delta(v - v') \exp(-\Delta\ell/\ell_c) + \left[1 - \exp(-\Delta\ell/\ell_c)\right] p_\ell(v). \tag{B2}$$

Inserting the latter into (B1) gives

$$\begin{aligned} f(t, v; \ell + \Delta\ell) = & f(t - \Delta\ell/v, v; \ell) \exp(-\Delta\ell/\ell_c) \\ & + \left[1 - \exp(-\Delta\ell/\ell_c)\right] p_\ell(v) \int_0^\infty \mathrm{d}v' f(t - v'/\Delta\ell, v'; \ell). \end{aligned} \tag{B3}$$

Expansion of the right side to linear order in $\Delta\ell$ gives

$$f(t, v; \ell + \Delta\ell) = f(t, v; \ell)(1 - \Delta\ell\kappa_c) - \frac{\Delta\ell}{v} \frac{\partial f(t, v; \ell)}{\partial t} + \Delta\ell\kappa_c p_\ell(v) \int_0^\infty \mathrm{d}v' f(t, v'; \ell), \tag{B4}$$

where we set $\kappa_c = 1/\ell_c$. The limit $\Delta\ell \to 0$ and isolating the time derivative of $f(t, v; \ell)$ gives equation (29).

## Appendix C: Graph Representation

We adopt a graph representation where vertices in the graph correspond to fractures in and edges correspond to intersections between fractures. Let $F = \{f_i\}$ for $i = 1, \ldots, N$ denote a fracture network composed of $n$ fractures. Every $f_i \in F$ is assigned a shape, location, and orientation within the domain by sampling distributions whose parameters are determined by a site characterization Every $f_i \in \mathbb{R}^2$ but the network $F \in \mathbb{R}^3$. Let $I = \{(f_i, f_j)\}$ be a set of pairs associated with intersections between fractures; if $f_i \cap f_j \neq \emptyset$, then $(f_i, f_j) \in I$. The number of intersections $M = |I|$ depends on the particular shape, orientation, and geometry of the set of fractures in the network. We denote the line of intersection between $f_i$ and $f_j$ as $\ell(f_i, f_j)$. Using these sets, the topology of a DFN can be defined as the tuple $(F, I)$.

The graph representation of the DFN $G(V, E)$ adopted here is a triple composed of (i) a set of vertices $V(G)$, (ii) a set of edges $E(G)$, and (iii) a relation that associates two vertices with each edge. For every $f_i \in F$, there is a unique vertex $u_i \in V$:

$$\phi : f_i \to u_i. \tag{C1}$$

If two fractures, $f_i$ and $f_j$ intersect, $(f_i,f_j) \in I$, then there is an edge in $E$ connecting the corresponding vertices,

$$\phi : (f_i, f_j) \in I \rightarrow e_{ij} = (u_i, u_j), \tag{C2}$$

where $(u, v) \in E$ denotes an edge between vertices $u$ and $v$. The graph is unweighted; both node and edge weights are uniform.

**Acknowledgments**
J. D. H. and A. H. are thankful for support from Department of Energy at Los Alamos National Laboratory under contract DE-AC52-06NA25 396 through the Laboratory-Directed Research and Development Program. J. D. H. acknowledges support from the LANL LDRD program office Grant 20180621ECR. M. D. gratefully acknowledges the support of the European Research Council (ERC) through the project MHetScale (617511). P. K. K. acknowledges a grant from Korea Environment Industry & Technology Institute(KEITI) through Subsurface Environmental Management (SEM) Project, funded by Korea Ministry of Environment(MOE; 2018002440003). DFNWORKS can be obtained at https://github.com/lanl/dfnWorks and run files for simulations can obtained at https://gitlab.com/hymanjd/hyman-jgr-2018.git.

## References

Abelin, H., Birgersson, L., Moreno, L., Widén, H., Ågren, T., & Neretnieks, I. (1991). A large-scale flow and tracer experiment in granite: 2. Results and interpretation. *Water Resources Research*, *27*(12), 3119–3135.

Abelin, H., Neretnieks, I., Tunbrant, S., & Moreno, L. (1985). Final report of the migration in a single fracture: Experimental results and evaluation. Nat. Genossenschaft fd Lagerung Radioaktiver Abfälle.

Albert, R., & Barabási, A. L. (2002). Statistical mechanics of complex networks. *Reviews of Modern Physics*, *74*(1), 47.

Andersson, J., & Dverstorp, B. (1987). Conditional simulations of fluid flow in three-dimensional networks of discrete fractures. *Water Resources Research*, *23*(10), 1876–1886.

Andresen, C. A., Hansen, A., Le Goc, R., Davy, P., & Hope, S. M. (2013). Topology of fracture networks. *Frontiers in Physics*, *1*, Art–7.

Barabási, A. L., & Albert, R. (1999). Emergence of scaling in random networks. *Science*, *286*(5439), 509–512.

Becker, M. W., & Shapiro, A. M. (2000). Tracer transport in fractured crystalline rock: Evidence of nondiffusive breakthrough tailing. *Water Resources Research*, *36*(7), 1677–1686.

Becker, M. W., & Shapiro, A. M. (2003). Interpreting tracer breakthrough tailing from different forced-gradient tracer experiment configurations in fractured bedrock. *Water Resources Research*, *39*(1), 1024. https://doi.org/10.1029/2001WR001190

Benke, R., & Painter, S. (2003). Modeling conservative tracer transport in fracture networks with a hybrid approach based on the Boltzmann transport equation. *Water Resources Research*, *39*(11), 1324. https://doi.org/10.1029/2003WR001966

Benson, D. A., Wheatcraft, S. W., & Meerschaert, M. M. (2000a). Application of a fractional advection-dispersion equation. *Water Resources Research*, *36*(6), 1403–1412.

Benson, D. A., Wheatcraft, S. W., & Meerschaert, M. M. (2000b). The fractional-order governing equation of Lévy motion. *Water Resources Research*, *36*(6), 1413–1423.

Berkowitz, B., & Balberg, I. (1993). Percolation theory and its application to groundwater hydrology. *Water Resources Research*, *29*(4), 775–794.

Berkowitz, B., Cortis, A., Dentz, M., & Scher, H. (2006). Modeling non-Fickian transport in geological formations as a continuous time random walk. *Reviews of Geophysics*, *44*, RG2003. https://doi.org/10.1029/2005RG000178

Berkowitz, B., & Scher, H. (1997a). Anomalous transport in random fracture networks. *Physical Review Letters*, *79*(20), 4038–4041.

Berkowitz, B., & Scher, H. (1997b). Anomalous transport in random fracture networks. *Physical Review Letters*, *79*(20), 4038.

Berkowitz, B., & Scher, H. (1998). Theory of anomalous chemical transport in random fracture networks. *Physical Review E*, *57*(5), 5858.

Berrone, S., Pieraccini, S., Scialò, S., & Vicini, F. (2015). A parallel solver for large scale DFN flow simulations. *SIAM Journal on Scientific Computing*, *37*(3), C285–C306.

Bisdom, K., Bertotti, G., & Nick, H. M. (2016). The impact of different aperture distribution models and critical stress criteria on equivalent permeability in fractured rocks. *Journal of Geophysical Research: Solid Earth*, *121*, 4045–4063. https://doi.org/10.1002/2015JB012657

Bogdanov, I., Mourzenko, V., Thovert, J. F., & Adler, P. (2007). Effective permeability of fractured porous media with power-law distribution of fracture sizes. *Physical Review E*, *76*(3), 036309.

Bonneau, F., Caumon, G., & Renard, P. (2016). Impact of a stochastic sequential initiation of fractures on the spatial correlations and connectivity of discrete fracture networks. *Journal of Geophysical Research: Solid Earth*, *121*, 5641–5658. https://doi.org/10.1002/2015JB012451

Bonnet, E., Bour, O., Odling, N. E., Davy, P., Main, I., Cowie, P., & Berkowitz, B. (2001). Scaling of fracture systems in geological media. *Reviews of Geophysics*, *39*(3), 347–383.

Bour, O., & Davy, P. (1997). Connectivity of random fault networks following a power law fault length distribution. *Water Resources Research*, *33*(7), 1567–1583.

Bour, O., & Davy, P. (1998). On the connectivity of three-dimensional fault networks. *Water Resources Research*, *34*(10), 2611–2622.

Cacas, M. C., Ledoux, E., Marsily, G. D., Tillie, B., Barbreau, A., Durand, E., & Peaudecerf, P. (1990). Modeling fracture flow with a stochastic discrete fracture network: Calibration and validation: 1. The flow model. *Water Resources Research*, *26*(3), 479–489.

Cardenas, M. B., Slottke, D. T., Ketcham, R. A., & Sharp, J. M. (2007). Navier-Stokes flow and transport simulations using real fractures shows heavy tailing due to eddies. *Geophysical Research Letters*, *34*, L14404. https://doi/org/10.1029/2007GL030545

Cardenas, M. B., Slottke, D. T., Ketcham, R. A., & Sharp, J. M. (2009). Effects of inertia and directionality on flow and transport in a rough asymmetric fracture. *Journal of Geophysical Research*, *114*, B06204. https://doi.org/10.1029/2009JB006336

Cirpka, O. A., & Kitanidis, P. K. (2000). An advective-dispersive streamtube approach for the transfer of conservative tracer data to reactive transport. *Water Resources Research*, *36*, 1209–1220.

Comolli, A., & Dentz, M. (2017). Anomalous dispersion in correlated porous media: A coupled continuous time random walk approach. *European Physical Journal B*, *90*(9), 166.

Cvetkovic, V. (2011). The tempered one-sided stable density: A universal model for hydrological transport? *Environmental Research Letters*, *6*(3), 34008.

Dagan, G., & Bressler, E. (1979). Solute dispersion in unsaturated soil at field scale: I. Theory. *Soil Science Society of America Journal*, *43*, 461–466.

Davy, P., Le Goc, R., & Darcel, C. (2013). A model of fracture nucleation, growth and arrest, and consequences for fracture density and scaling. *Journal of Geophysical Research: Solid Earth*, *118*, 1393–1407. https://doi.org/10.1002/jgrb.50120

de Dreuzy, J. R., Darcel, C., Davy, P., & Bour, O. (2004). Influence of spatial correlation of fracture centers on the permeability of two-dimensional fracture networks following a power law length distribution. *Water Resources Research*, *40*, W01502. https://doi.org/10.1002/jgrb.50120

De Dreuzy, J., Davy, P., & Bour, O. (2000). Percolation threshold of 3D random ellipses with widely-scattered distributions of eccentricity and size. *Physical Review E*, *62*(5), 5948–5952.

de Dreuzy, J. R., Davy, P., & Bour, O. (2001). Hydraulic properties of two-dimensional random fracture networks following a power law length distribution 2. Permeability of networks based on lognormal distribution of apertures. *Water Resources Research*, *37*(8), 2079–2095.

de Dreuzy, J. R., Davy, P., & Bour, O. (2002). Hydraulic properties of two-dimensional random fracture networks following power law distributions of length and aperture. *Water Resources Research*, *38*(12), 1276. https://doi.org/10.1029/2001WR001009

de Dreuzy, J. R., Méheust, Y., & Pichot, G. (2012). Influence of fracture scale heterogeneity on the flow properties of three-dimensional discrete fracture networks. *Journal of Geophysical Research*, *117*, B11207. https://doi.org/10.1029/2012JB009461

Dentz, M., Kang, P., Comolli, A., Le Borgne, T., & Lester, D. R. (2016). Continuous time random walks for the evolution of Lagrangian velocities. *Physical Review Fluids*, *1*(7), 074004.

Dershowitz, W., & Fidelibus, C. (1999). Derivation of equivalent pipe network analogues for three-dimensional discrete fracture networks by the boundary element method. *Water Resources Research*, *35*(9), 2685–2691.

Di Donato, G., Obi, E. O., & Blunt, M. J. (2003). Anomalous transport in heterogeneous media demonstrated by streamline-based simulation. *Geophysical Research Letters*, *30*(12), 1608. https://doi.org/10.1029/2003GL017196

Dijkstra, E. W. (1959). A note on two problems in connexion with graphs. *Numerische Mathematic*, *1*(1), 269–271.

Edery, Y., Geiger, S., & Berkowitz, B. (2016). Structural controls on anomalous transport in fractured porous rock. *Water Resources Research*, *52*, 5634–5643. https://doi.org/10.1002/2016WR018942

Erhel, J., de Dreuzy, J. R., & Poirriez, B. (2009). Flow simulation in three-dimensional discrete fracture networks. *SIAM Journal on Scientific Computing*, *31*(4), 2688–2705.

Fiori, A., & Becker, M. W. (2015). Power law breakthrough curve tailing in a fracture: The role of advection. *Journal of Hydrology*, *525*, 706–710.

Follin, S., Hartley, L., Rhén, I., Jackson, P., Joyce, S., Roberts, D., & Swift, B. (2014). A methodology to constrain the parameters of a hydrogeological discrete fracture network model for sparsely fractured crystalline rock, exemplified by data from the proposed high-level nuclear waste repository site at Forsmark, Sweden. *Hydrogeology Journal*, *22*(2), 313–331.

Frampton, A., & Cvetkovic, V. (2007). Upscaling particle transport in discrete fracture networks: 1. Nonreactive tracers. *Water Resources Research*, *43*, W10428. https://doi.org/10.1029/2006WR005334

Frampton, A., & Cvetkovic, V. (2009). Significance of injection modes and heterogeneity on spatial and temporal dispersion of advecting particles in two-dimensional discrete fracture networks. *Advances in Water Resources*, *32*(5), 649–658.

Frampton, A., & Cvetkovic, V. (2010). Inference of field-scale fracture transmissivities in crystalline rock using flow log measurements. *Water Resources Research*, *46*, W11502. https://doi.org/10.1029/2009WR008367

Frampton, A., & Cvetkovic, V. (2011). Numerical and analytical modeling of advective travel times in realistic three-dimensional fracture networks. *Water Resources Research*, *47*, W02506. https://doi.org/10.1029/2010WR009290

Ginn, T. R., Simmons, C. S., & Wood, B. D. (1995). Stochastic-convective transport with nonlinear reaction: Biodegradation with microbial growth. *Water Resources Research*, *31*(11), 2689–2700.

Gouze, P., Le Borgne, T., Leprovost, R., Lods, G., Poidras, T., & Pezard, P. (2008). Non-Fickian dispersion in porous media: 1. Multiscale measurements using single-well injection withdrawal tracer tests. *Water Resources Research*, *44*, W06427. https://doi.org/10.1029/2007WR006278

Hadermann, J., & Heer, W. (1996). The Grimsel (Switzerland) migration experiment: Integrating field experiments, laboratory investigations and modellin. *Journal of Contaminant Hydrology*, *21*(1-4), 87–100.

Haggerty, R., & Gorelick, S. M. (1995). Multiple-rate mass transfer for modeling diffusion and surface reactions in media with pore-scale heterogeneity. *Water Resources Research*, *31*(10), 2383–2400.

Hamzehpour, H., Mourzenko, V., Thovert, J. F., & Adler, P. (2009). Percolation and permeability of networks of heterogeneous fractures. *Physical Review E*, *79*(3), 036302.

Hardebol, N., Maier, C., Nick, H., Geiger, S., Bertotti, G., & Boro, H. (2015). Multiscale fracture network characterization and impact on flow: A case study on the Latemar carbonate platform. *Journal of Contaminant Hydrology*, *120*(12), 8197–8222.

Hope, S. M., Davy, P., Maillot, J., Le Goc, R., & Hansen, A. (2015). Topological impact of constrained fracture growth. *Frontiers in Physics*, *3*, 75.

Huseby, O., Thovert, J., & Adler, P. (1997). Geometry and topology of fracture systems. *Journal of Physics A: Mathematical and General*, *30*(5), 1415.

Huseby, O., Thovert, J. F., & Adler, P. (2001). Dispersion in three-dimensional fracture networks. *Physics of Fluids*, *13*(3), 594–615.

Hyman, J. D., Aldrich, G., Viswanathan, H., Makedonska, N., & Karra, S. (2016). Fracture size and transmissivity correlations: Implications for transport simulations in sparse three-dimensional discrete fracture networks following a truncated power law distribution of fracture size. *Water Resources Research*, *52*, 6472–6489. https://doi.org/10.1002/2016WR018806

Hyman, J. D., Gable, C. W., Painter, S. L., & Makedonska, N. (2014). Conforming Delaunay triangulation of stochastically generated three dimensional discrete fracture networks: A feature rejection algorithm for meshing strategy. *SIAM Journal on Scientific Computing*, *36*(4), A1871–A1894.

Hyman, J. D., Hagberg, A., Osthus, D., Srinivasan, S., Viswanathan, H., & Srinivasan, G. (2018). Identifying backbones in three-dimensional discrete fracture networks: A bipartite graph-based approach. *Multiscale Modeling & Simulation*, *16* (4), 1948–1968.

Hyman, J. D., Hagberg, A., Srinivasan, G., Mohd-Yusof, J., & Viswanathan, H. (2017). Predictions of first passage times in sparse discrete fracture networks using graph-based reductions. *Physical Review E*, *96*(1), 013304. https://doi.org/10.1103/PhysRevE.96.013304

Hyman, J. D., & Jiménez-Martínez, J. (2018). Dispersion and mixing in three-dimensional discrete fracture networks: Nonlinear interplay between structural and hydraulic heterogeneity. *Water Resources Research*, *54*, 3243–3258. https://doi.org/10.1029/2018WR022585

Hyman, J. D., Jiménez-Martínez, J., Viswanathan, H., Carey, J., Porter, M., Rougier, E., & Makedonska, N. (2016). Understanding hydraulic fracturing: A multi-scale problem. *Philosophical Transactions of the Royal Society A*, *374*(2078), 20150426.

Hyman, J. D., Karra, S., Makedonska, N., Gable, C. W., Painter, S. L., & Viswanathan, H. S. (2015). Works: A discrete fracture network framework for modeling subsurface flow and transport. *Computers & Geosciences*, *84*, 10–19.

Hyman, J. D., Painter, S. L., Viswanathan, H., Makedonska, N., & Karra, S. (2015). Influence of injection mode on transport properties in kilometer-scale three-dimensional discrete fracture networks. *Water Resources Research*, *51*, 7289–7308. https://doi.org/10.1002/2015WR017151

Jenkins, C., Chadwick, A., & Hovorka, S. D. (2015). The state of the art in monitoring and verification—Ten years on. *International Journal of Greenhouse Gas Control*, *40*, 312–349.

Johnson, J., Brown, S., & Stockman, H. (2006). Fluid flow and mixing in rough-walled fracture intersections. *Journal of Geophysical Research*, *111*, B12206. https://doi.org/10.1029/2005JB004087

Joyce, S., Hartley, L., Applegate, D., Hoek, J., & Jackson, P. (2014). Multi-scale groundwater flow modeling during temperate climate conditions for the safety assessment of the proposed high-level nuclear waste repository site at Forsmark, Sweden. *Hydrogeology Journal*, *22*(6), 1233–1249.

Kang, P. K., Brown, S., & Juanes, R. (2016). Emergence of anomalous transport in stressed rough fractures. *Earth and Planetary Science Letters*, *454*, 46–54.

Kang, P. K., Dentz, M., Le Borgne, T., & Juanes, R. (2011). Spatial Markov model of anomalous transport through random lattice networks. *Physical Review Letters*, *107*, 180602.

Kang, P. K., Dentz, M., Le Borgne, T., Lee, S., & Juanes, R. (2017). Anomalous transport in disordered fracture networks: Spatial Markov model for dispersion with variable injection modes. *Advances in Water Resources*, *106*, 80–94.

Kang, P. K., Le Borgne, T., Dentz, M., Bour, O., & Juanes, R. (2015). Impact of velocity correlation and distribution on transport in fractured media: Field evidence and theoretical model. *Water Resources Research*, *51*, 940–959. https://doi.org/10.1002/2014WR015799

Karra, S., Makedonska, N., Viswanathan, H., Painter, S., & Hyman, J. D. (2015). Effect of advective flow in fractures and matrix diffusion on natural gas production. *Water Resources Research*, *51*, 8646–8657. https://doi.org/10.1002/2014WR016829

Keller, A. A., Roberts, P. V., & Blunt, M. J. (1999). Effect of fracture aperture variations on the dispersion of contaminants. *Water Resources Research*, *35*(1), 55–63.

Keller, A. A., Roberts, P. V., & Kitanidis, P. K. (1995). Prediction of single phase transport parameters in a variable aperture fracture. *Geophysical Research Letters*, *22*(11), 1425–1428.

Koponen, A., Kataja, M., & Timonen, J. (1996). Tortuous flow in porous media. *Pysical Review E*, *54*(1), 406.

Koudina, N., Garcia, R. G., Thovert, J. F., & Adler, P. (1998). Permeability of three-dimensional fracture networks. *Physical Review E*, *57*(4), 4466.

Kreft, A., & Zuber, A. (1978). On the physical meaning of the dispersion equation and its solutions for different initial and boundary conditions. *Chemical Engineering Science*, *33*, 1471–1480.

Kueper, B. H., & McWhorter, D. B. (1991). The behavior of dense, nonaqueous phase liquids in fractured clay and rock. *Ground Water*, *29*(5), 716–728.

LaGriT (2013). Los Alamos Grid Toolbox, (LaGriT), Los Alamos National Laboratory, http://lagrit.lanl.gov

Lang, P., Paluszny, A., & Zimmerman, R. (2014). Permeability tensor of three-dimensional fractured porous rock and a comparison to trace map predictions. *Journal of Geophysical Research: Solid Earth*, *119*, 6288–6307. https://doi.org/10.1002/2014JB011027

Le Borgne, T., Dentz, M., & Carrera, J. (2008a). A Lagrangian statistical model for transport in highly heterogeneous velocity fields. *Physical Review Letters*, *101*, 90601.

Le Borgne, T., Dentz, M., & Carrera, J. (2008b). Spatial Markov processes for modeling Lagrangian particle dynamics in heterogeneous porous media. *Physical Review E*, *78*, 41110.

Lichtner, P., Hammond, G., Lu, C., Karra, S., Bisht, G., Andre, B., & Kumar, J. (2015). PFLOTRAN user manual: A massively parallel reactive flow and transport model for describing surface and subsurface processes, (Report No.: LA-UR-15-20403) Los Alamos National Laboratory.

Long, J., Remer, J., Wilson, C., & Witherspoon, P. (1982). Porous media equivalents for networks of discontinuous fractures. *Water Resources Research*, *18*(3), 645–658.

Maillot, J., Davy, P., Le Goc, R., Darcel, C., & De Dreuzy, J. R. (2016). Connectivity, permeability, and channeling in randomly distributed and kinematically defined discrete fracture network models. *Water Resources Research*, *52*, 8526–8545. https://doi.org/10.1002/2016WR018973

Makedonska, N., Hyman, J. D., Karra, S., Painter, S. L., Gable, C. W. W., & Viswanathan, H. S. (2016). Evaluating the effect of internal aperture variability on transport in kilometer scale discrete fracture networks. *Advances in Water Resources*, *94*, 486–497.

Makedonska, N., Painter, S. L., Bui, Q. M., Gable, C. W., & Karra, S. (2015). Particle tracking approach for transport in three-dimensional discrete fracture networks. *Computational Geosciences*, *19*, 1123–1137.

Massoudieh, A. M., Dentz, M., & Alikhani, J. (2017). A spatial Markov model for the evolution of the joint distribution of groundwater age, arrival time, and velocity in heterogeneous media. *Water Resources Research*, *53*, 5495–5515. https://doi.org/10.1002/2017WR020578

Middleton, R., Carey, J., Currier, R., Hyman, J. D., Kang, Q., Karra, S., & Viswanathan, H. (2015). Shale gas and non-aqueous fracturing fluids: Opportunities and challenges for supercritical $CO_2$. *Applied Energy*, *147*, 500–509.

Mourzenko, V., Thovert, J. F., & Adler, P. (2004). Macroscopic permeability of three-dimensional fracture networks with power-law size distribution. *Physical Review E*, *69*(6), 66307.

Mourzenko, V., Thovert, J. F., & Adler, P. (2005). Percolation of three-dimensional fracture networks with power-law size distribution. *Physical Review E*, *72*(3), 36103.

Mourzenko, V. V., Thovert, J. F., & Adler, P. M. (2011). Permeability of isotropic and anisotropic fracture networks, from the percolation threshold to very large densities. *Physical Review E*, *84*(3), 036307.

National Research Council (1996). Rock fractures and fluid flow: Contemporary understanding and applications. U. C. on Fracture Characterization, F. Flow, National Academy Press.

Neuman, S. (2005). Trends, prospects and challenges in quantifying flow and transport through fractured rocks. *Hydrogeology Journal*, *13*(1), 124–147.

Neuman, S. P., & Tartakovsky, D. M. (2009). Perspective on theories of non-Fickian transport in heterogeneous media. *Advances in Water Resources*, *32*(5), 670–680.

Newman, M. E. (2002). Assortative mixing in networks. *Physical Review Letters*, *89*(20), 208701.

Newman, M. E. (2003). Mixing patterns in networks. *Physical Review E*, *67*(2), 026126.

Noetinger, B., Roubinet, D., Russian, A., Le Borgne, T., Delay, F., Dentz, M., & Gouze, P. (2016). Random walk methods for modeling hydrodynamic transport in porous and fractured media from pore to reservoir scale. *Transport in Porous Media*, *115*, 345–385.

Nordqvist, A. W., Tsang, Y., Tsang, C., Dverstorp, B., & Andersson, J. (1992). A variable aperture fracture network model for flow and transport in fractured rocks. *Water Resources Research*, *28*(6), 1703–1713.

Painter, S., Cvetkovic, V., & Selroos, J. O. (2002). Power-law velocity distributions in fracture networks: Numerical evidence and implications for tracer transport. *Geophysical Research Letters*, *29*(14), 1676. https://doi.org/10.1029/2002GL014960

Painter, S. L., Gable, C. W., & Kelkar, S. (2012). Pathline tracing on fully unstructured control-volume grids. *Computational Geosciences*, *16*(4), 1125–1134.

Rasmuson, A., & Neretnieks, I. (1986). Radionuclide transport in fast channels in crystalline rock. *Water Resources Research*, *22*(8), 1247–1256.

Sahimi, M. (1994). *Applications of percolation theory*. Boca Raton, FL: CRC Press.

Selroos, J. O., Walker, D. D., Ström, A., Gylling, B., & Follin, S. (2002). Comparison of alternative modelling approaches for groundwater flow in fractured rock. *Journal of Hydrology*, *257*(1-4), 174–188.

Valera, M., Guo, Z., Kelly, P., Matz, S., Cantu, V. A., Percus, A. G., & Viswanathan, H. S. (2018). Machine learning for graph-based representations of three-dimensional discrete fracture networks. *Computational Geosciences*, *22*(3), 695–710. https://doi.org/10.1007/s10596-018-9720-1

VanderKwaak, J., & Sudicky, E. (1996). Dissolution of non-aqueous-phase liquids and aqueous-phase contaminant transport in discretely-fractured porous media. *Journal of Contaminant Hydrology*, *23*(1-2), 45–68.

Wellman, T. P., Shapiro, A. M., & Hill, M. C. (2009). Effects of simplifying fracture network representation on inert chemical migration in fracture-controlled aquifers. *Water Resources Research*, *45*, W01416. https://doi.org/10.1029/2008WR007025

Witherspoon, P. A., Wang, J., Iwai, K., & Gale, J. (1980). Validity of cubic law for fluid flow in a deformable rock fracture. *Water Resources Research*, *16*(6), 1016–1024.

Zou, L., Jing, L., & Cvetkovic, V. (2017). Modeling of solute transport in a 3D rough-walled fracture—Matrix system. *Transport in Porous Media*, *116*(3), 1005–1029. https://doi.org/10.1007/s11242-016-0810-z